American Mineralogist, Volume 76, pages 971–984, 1991

Exsolution of cummingtonite from glaucophane: A new orientation for exsolution lamellae in clinoamphiboles

Eugene A. Smelik, David R. Veblen
Department of Earth and Planetary Sciences, The Johns Hopkins University, Baltimore, Maryland 21218, U.S.A.

Abstract

Samples of glaucophane from eclogite assemblages in northern Vermont have been studied using transmission and analytical electron microscopy (TEM, AEM). The results show that the glaucophane is exsolved on a submicroscopic scale and contains abundant lamellae of cummingtonite. AEM analyses indicate that the present pair of coexisting sodic-ferromagnesian amphiboles differs significantly from all previously reported pairs and represents the first report of coexisting glaucophane-cummingtonite from normal eclogitic assemblages.

The lamellae are disc shaped and are coherently intergrown with the host. They occur in two symmetrically related orientations, nearly parallel to $(28\bar{1})$ and $(2\bar{8}\bar{1})$ planes of the host. Optimal phase boundary calculations indicate that these orientations represent planes of best dimensional fit between the glaucophane and cummingtonite lattices. This orientation differs significantly from previously reported lamellar orientations for monoclinic amphiboles, which generally occur nearly parallel to $(\bar{1}01)$ and (100) planes for the $C2/m$ unit-cell setting.

Introduction

During the last two decades, there has been a considerable effort made toward understanding miscibility gaps between different amphibole series. Research has shown that compositional gaps exist between all pairs of the four (sodic, sodic-calcic, calcic, and ferromagnesian) major amphibole subgroups of Leake (1978) (Ghose, 1981; Robinson et al., 1982; Smelik and Veblen, 1989). Evidence cited for miscibility gaps between major amphibole end-members includes coexisting amphibole grains that grew under equilibrium conditions and the observation of oriented exsolution lamellae of one amphibole in another. Exsolution among calcic and ferromagnesian amphiboles and in the orthoamphibole (gedrite-anthophyllite) system has been widely reported, and these miscibility gaps have been delineated by many workers (e.g., Vernon, 1962; Robinson, 1963; Jaffe et al., 1968; Robinson et al., 1969; Ross et al., 1969; Robinson and Jaffe, 1969; Robinson et al., 1971a; Stout 1970, 1971, 1972; Gittos et al., 1974, 1976; Spear, 1980, 1982). Exsolution between sodic and ferromagnesian amphiboles has been reported by Klein (1966, 1968) in metasedimentary rocks from Labrador and by Ghose et al. (1974) and Shau et al. (1989) in Mn-rich rocks from Tirodi, Maharashtra, India. Other authors have reported coexisting coarse-grained sodic and ferromagnesian amphiboles (Black, 1973; Kimball and Spear, 1984).

This paper describes new evidence for immiscibility between sodic and ferromagnesian amphiboles and discusses (1) exsolution of cummingtonite in common eclogitic glaucophane and (2) a new crystallographic orientation for exsolution lamellae in monoclinic amphiboles, which can be rationalized by optimal phase boundary arguments.

Geologic setting of samples

The glaucophane samples examined in this study are part of a type C eclogite assemblage described by Bothner and Laird (1987). These eclogites occur at a locality known as Eclogite Brook in north-central Vermont (see Fig. 5 in Bothner and Laird, 1987). They belong to the Belvidere Mountain Amphibolite Member of the Hazens Notch Formation (nomenclature from Doll et al., 1961) and are structurally related to the more abundant outcrops of blueschist that occur several kilometers to the south at Tillotson Peak (Bothner and Laird, 1987).

Evidence of high-pressure metamorphism in the mafic schists at Tillotson Peak was first recognized by Laird (1977). Detailed electron microprobe analyses of the minerals in these rocks were presented by Laird and Albee (1981a), who reported the occurrence of three different amphiboles: glaucophane, actinolite, and barroisite (classification of Leake, 1978). In a subsequent paper, Laird and Albee (1981b) used changing mineral compositions in mafic schists from Tillotson Peak and a variety of other locations to help unravel the complicated polymetamorphic history of Vermont. From their analysis, they have identified four major periods of metamorphism affecting the Paleozoic rocks of Vermont (see Laird and Albee, 1981b, Table 3, p. 160–161).

Two major events (O1, O2) affecting Cambrian to Ordovician samples occurred during the Ordovician (Ta-

0003–004X/91/0506–0971$02.00

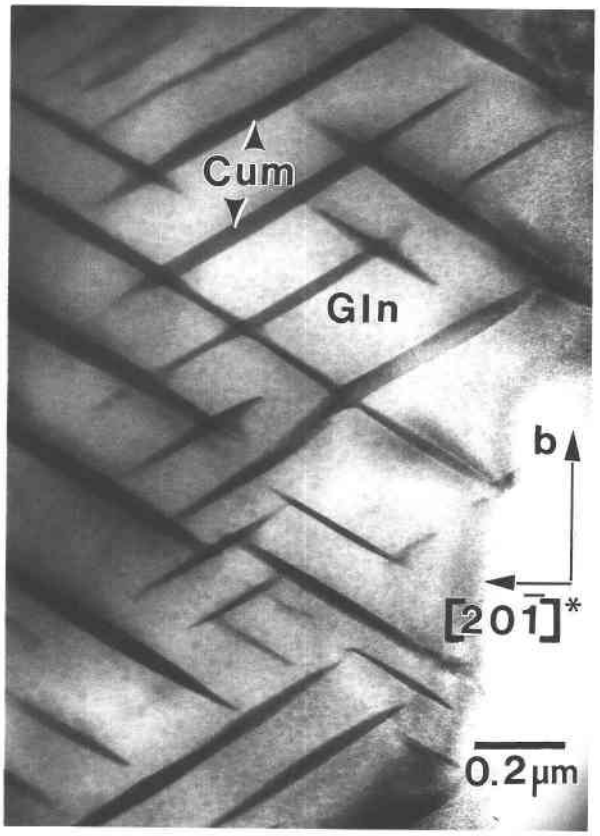

Fig. 1. Low-magnification TEM image of exsolved glaucophane grain. Note that lamellae of cummingtonite occur in two orientations and vary in size, reaching a maximum thickness of about 60 nm. The electron beam is parallel to [102] of the host.

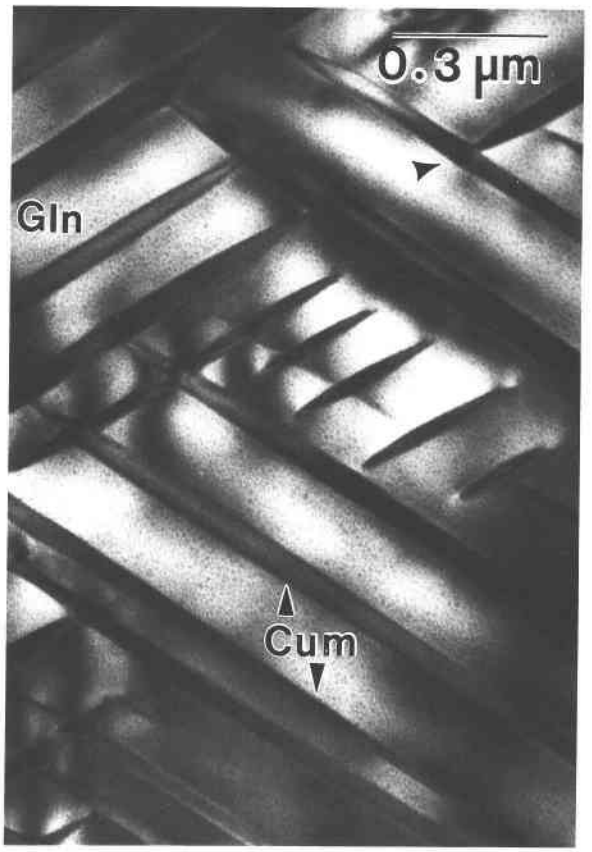

Fig. 2. TEM image of cummingtonite lamellae in glaucophane. Several smaller lamellae have grown in areas between coarser lamellae, indicating progressive stages of exsolution with decreasing temperature. Note that some lamellae bulge slightly at the approach of other lamellae (arrow). Coherency strain is also evident at some of the lamellar tips. The orientation is the same as Figure 1 with **b** vertical and [20$\bar{1}$]* horizontal. The electron beam is parallel to [102] of the host.

conic Orogeny). Each of these is characterized by high-pressure facies metamorphism in some areas and by medium-pressure facies in other areas (Laird and Albee, 1981b). The O2 event has been dated by Lanphere and Albee (1974) and assigned an isotopic age of 463 ± 43 m.y. No absolute age has been determined for the earlier event, O1.

Two metamorphic events (D1, D2) also occurred during the Devonian (Acadian Orogeny). The first (D1) is characterized by low-pressure facies metamorphism in Devonian rocks and by medium-pressure facies metamorphism in Cambrian to Ordovician samples. The second is characterized by low-pressure facies metamorphism in Cambrian to Devonian samples (Laird and Albee, 1981b).

The minerals in the Eclogite Brook rocks reflect high-pressure metamorphism assigned by Laird and Albee (1981b) to the Ordovician events. The cores of discontinuously zoned amphibole grains are thought to have grown during the O1 event, and the rims plus optically continuous grains have been assigned to the O2 event.

Specimen description and experimental technique

Specimens for transmission electron microscopy (TEM) experiments were made from 30 μm thin sections taken from Eclogite Brook samples (see locality 2 of Bothner and Laird, 1987, Fig. 5). The glaucophane generally occurs in clots adjacent to layers of garnet porphyroblasts. The glaucophane is usually lavender to blue in color and is sometimes strongly pleochroic. Although some grains are zoned with darker-blue cores, none of the glaucophane crystals show any evidence of exsolution lamellae when examined with the petrographic microscope.

Several TEM samples were prepared by ion thinning selected areas of petrographic thin sections. Petrographic examination of ion-thinned edges revealed subtle refractive index discontinuities that might reflect inhomogeneities in the samples. Electron microscopy was performed with a Philips EM420 transmission electron microscope operated at 120 keV. Both a Supertwin (ST) objective

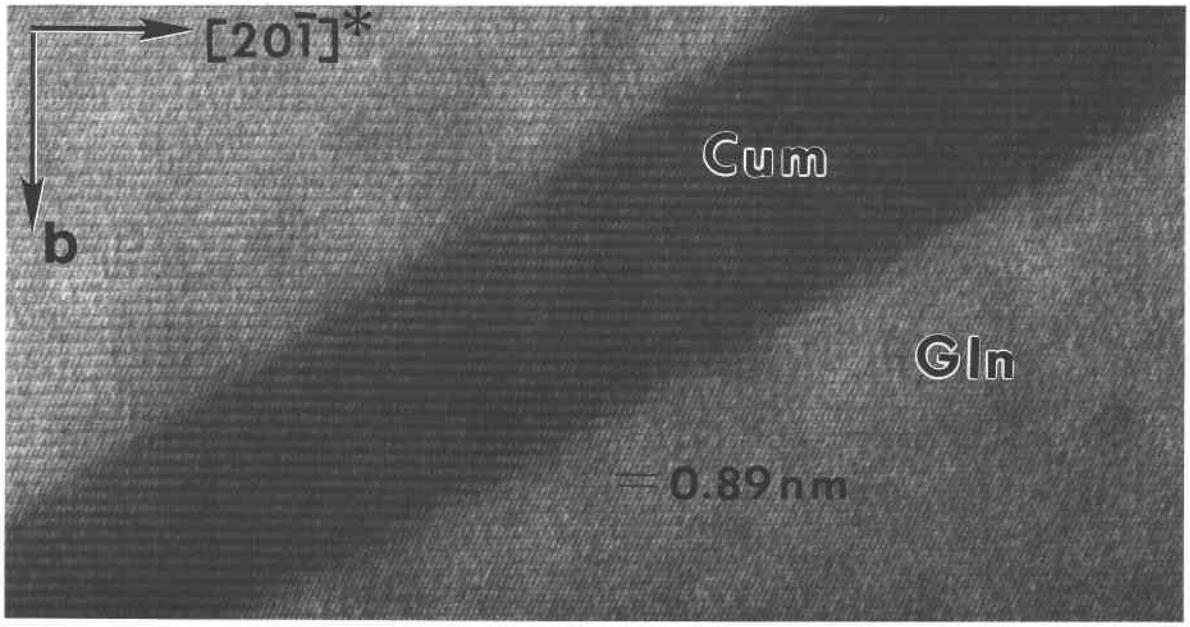

Fig. 3. HRTEM image of host-lamellar interfaces. The (020) lattice fringes for the glaucophane (≈0.89 nm) and cummingtonite (≈0.907 nm) are coherent across the interface with very little distortion at the phase boundary (viewed best at a low angle). The electron beam is parallel to [102] of the host.

lens (spherical aberration coefficient C_s = 1.2 mm, chromatic aberration coefficient C_c = 1.2 mm) and a Twin (T) objective lens (C_s = 2.0 mm, C_c = 2.0 mm) were employed. For HRTEM imaging, the objective aperture diameter either matched the point resolution of the microscope (0.30 nm for the ST lens and 0.34 nm for the T lens) or was smaller in order to eliminate irrelevant high-frequency information from the images.

Energy dispersive X-ray spectra were collected with an EDAX SiLi detector and processed with a Princeton Gamma-Tech model 4000 analyzer, as described by Livi and Veblen (1987).

Distribution and morphology of exsolution lamellae

As noted above, there was no obvious evidence of exsolution lamellae in the glaucophane crystals when examined with the petrographic microscope, although variations in optical properties were observed in ion-thinned edges. When examined with the TEM, the glaucophane crystals were found to contain abundant, submicroscopic exsolution lamellae of a second phase (Figs. 1 and 2). The lamellae occur in two orientations (see discussion on lamellar orientation below) and are coherent with the host (Fig. 3). The coarsest exsolution textures observed are like those shown in Figures 1 and 2, with lamellae reaching a maximum thickness of about 60 nm and a maximum length (in cross section) of about 2.5 μm. In many cases, smaller lamellae have grown in regions between larger lamellae (Figs. 1 and 2). In rarer cases, Guinier-Preston (GP) zones have formed in supersaturated areas between coarse lamellae (Fig. 4), similar to the GP zones observed in some pyroxene samples (e.g., Nord, 1980). The wide range of lamellar sizes in these samples suggests progressive stages of exsolution in the glaucophane as the rocks cooled.

In general, interfaces between the lamellae and host are close to planar and are coherent (Fig. 3). TEM images of fine-scale exsolution lamellae reveal the lamellae to be disc-shaped precipitates that taper at both ends when viewed in cross section. It is also common to observe bulging of one lamella as it is approached by others (see Figs. 1, 2, and 5). This bulging of lamellae is commonly observed in pyroxene (e.g., Rietmeijer and Champness, 1982; Kitamura, 1981) and may be caused, in part, by strain field interactions between the growing lamellae (Livi and Veblen, 1989).

Amphibole chemical relations

Cummingtonite

Using a fine probe (diameter ≈ 10–20 nm), analyses of both the host and lamellae were obtained. Because the exsolution lamellae are quite narrow (Figs. 1, 2, and 5), analysis proved difficult in many cases, in particular when tilting the specimen for optimum take-off angle toward the EDS detector resulted in significant tilting of the lamellae with respect to the electron beam. In this situation, there was an increased possibility for the lamella spectrum to contain contributions from the host mineral. The best analyses were obtained when the tilt for optimum take-off angle also brought the lamellae fortuitously

Fig. 4. TEM image of GP zones in the area between coarse cummingtonite lamellae. These tiny platelets probably nucleated homogeneously in an area that has become supersaturated with respect to Fe-Mg. Precipitate-free zones can be seen adjacent to the larger lamellae. A nonzone-axis orientation was used to enhance contrast.

into a nearly edge-on orientation. Representative analytical electron microscopy (AEM) analyses of the lamellae are presented in Table 1. These analyses clearly show that, according to the criteria of Leake (1978), the lamellae are ferromagnesian amphibole. Selected-area electron diffraction (SAED) patterns indicating $C2/m$ symmetry further identify the lamellae as cummingtonite.

Results from single-crystal X-ray diffraction studies (Ghose, 1961; Fischer, 1966; Finger, 1969) and Mössbauer spectroscopy (Bancroft et al., 1967a, 1967b; Hafner and Ghose, 1971) have shown that most iron magnesium manganese amphiboles in the cummingtonite-grunerite series contain little Fe^{3+} and that Fe^{2+} is strongly ordered into the M4 site. The structural formulae of the cummingtonite lamellae, therefore, have been calculated on a 23–O atom basis assuming all Fe to be present as FeO. From Table 1, it is evident that the cummingtonite lamellae contain a significant glaucophane component, with 0.102–0.213 Na assigned to the M4 site and 0.014–0.119 Al in octahedral coordination, probably at the M2 site (Papike and Clark, 1968). This apparent glaucophane component may be due to small contributions from the glaucophane host that entered into the analyses, or it may reflect a small degree of actual solid solution between glaucophane and cummingtonite. The ratio of Mg/(Mg + Fe^{2+}) in the cummingtonite ranged from 0.559 to 0.652 with an overall average of 0.589. Using this recalculation scheme, the A-site occupancy was generally low but reached about ⅓ in several cases. It should be noted that the low accuracy of these AEM analyses compared to electron microprobe analyses can result in a wide range of apparent A-site occupancy for amphiboles and these numbers should be considered with caution. The analyses also show small amounts of Ca that have been assigned to the M4 site. These cummingtonite lamellae have significantly lower Ca content than cummingtonite lamellae

Table 1. Representative AEM analyses for cummingtonite lamellae

		Amphibole formula: based on normalization to 23 O atoms and assuming all Fe as FeO							
Sample no.		VEB1-H	VEB1-H	VEB1-A	VEB1-A	VEB1-A	VEB1-A	VEB1-H	VEB1-H
Spectrum no.		EBH6B	EBH7B	EAC1B	EAC5B	EAC6B	EAC9B	EBH4B	EBH5B
Tetrahedral	Si	7.91	7.91	7.83	7.78	7.76	7.86	7.93	7.96
	Al	0.09	0.09	0.17	0.22	0.24	0.14	0.07	0.04
	Total T-site	8.00	8.00	8.00	8.00	8.00	8.00	8.00	8.00
Octahedral	Al	0.07	0.12	0.11	0.01	0.09	0.10	0.04	0.06
M1, M2, M3	Ti	0.01	0.00	0.01	0.00	0.00	0.00	0.00	0.00
	Cr	0.01	0.00	0.00	0.00	0.00	0.00	0.00	0.00
	Mg	3.72	3.74	3.93	3.94	4.04	3.90	3.93	3.77
	Fe^{2+}	1.18	1.14	0.96	1.05	0.87	0.99	1.04	1.16
	Total M1–M3	4.99	5.00	5.01	5.00	5.00	4.99	5.01	4.99
Octahedral	Ca	0.11	0.12	0.10	0.11	0.11	0.11	0.05	0.05
M4	Na	0.19	0.16	0.21	0.10	0.17	0.17	0.15	0.14
	Fe^{2+}	1.69	1.72	1.68	1.79	1.70	1.71	1.80	1.82
	Mn	0.01	0.00	0.01	0.00	0.02	0.01	0.00	0.00
	Total M4	2.00	2.00	2.00	2.00	2.00	2.00	2.00	2.01
A site	Na	0.16	0.12	0.25	0.31	0.30	0.21	0.18	0.11
	K	0.02	0.01	0.01	0.00	0.01	0.00	0.00	0.00
	Total A site	0.18	0.13	0.26	0.31	0.31	0.21	0.18	0.11
Mg/(Mg + Fe^{2+})		0.564	0.567	0.598	0.581	0.611	0.591	0.580	0.559

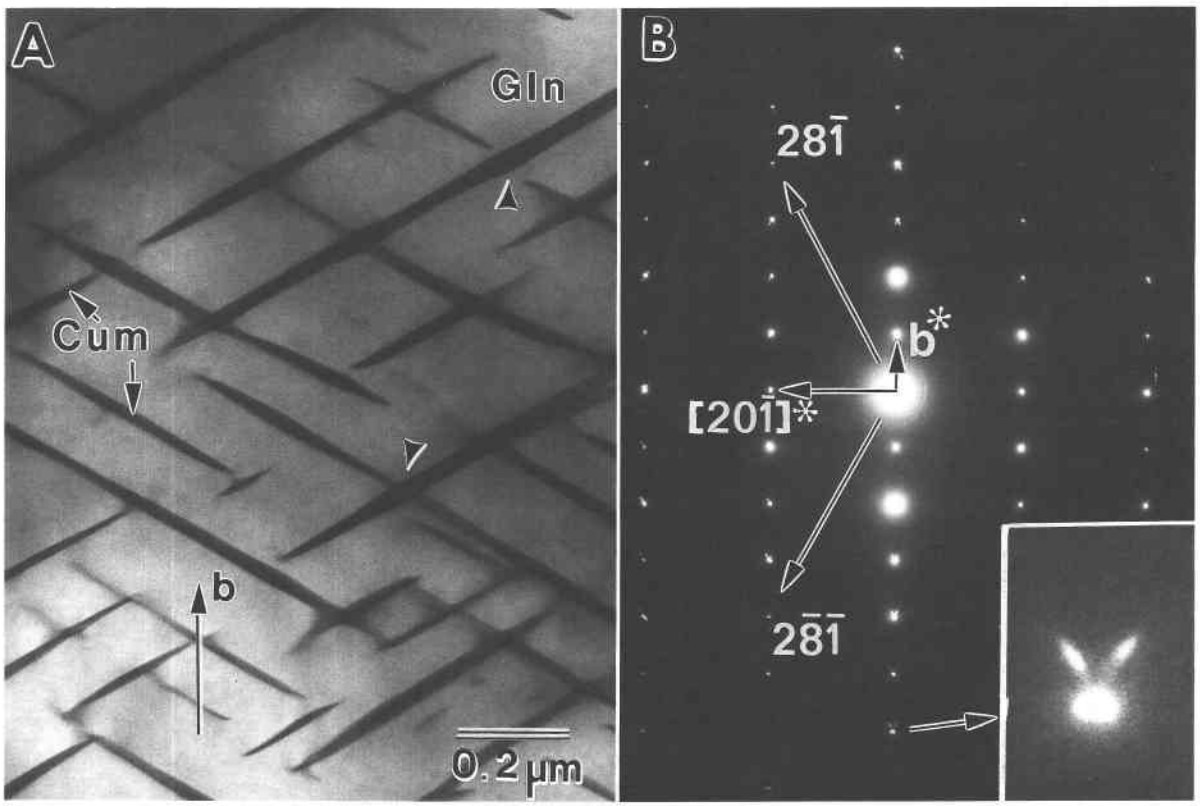

Fig. 5. Orientation of cummingtonite lamellae. (**A**) TEM image of cummingtonite lamellae viewed in cross section down [102] of the host. Note the sharp interfaces between lamellae and host and that some lamellae bulge slightly at the approach of other lamellae (arrows). (**B**) Corresponding SAED pattern of the [102] zone showing the **b***-[20$\bar{1}$]* reciprocal lattice plane. Also labeled are the (28$\bar{1}$) and (2$\bar{8}\bar{1}$) reflections and corresponding reciprocal lattice vectors. Note that the [28$\bar{1}$]* vector is nearly perpendicular to one set of lamellae and [2$\bar{8}\bar{1}$]* is nearly perpendicular to the other, indicating that the lamellae are nearly parallel to these respective lattice planes and that these orientations are symmetrically related by the mirror plane perpendicular to **b**. Close examination of the diffraction spots reveals distinctive splitting caused by the cummingtonite lamellae (inset). The left "rabbit ear" is formed by the "28$\bar{1}$" lamellae and the right one by the "2$\bar{8}\bar{1}$" lamellae. These spots are elongated perpendicular to the set of lamellae forming them because of the shape effect. The maximum axial component of splitting is parallel to **b***, indicating that the maximum dimensional difference between the glaucophane and cummingtonite lattice is in the **b** axis.

in nearby blueschist glaucophanes, which have developed secondary exsolution lamellae of actinolite (Smelik and Veblen, 1989).

Glaucophane

Analyses of the glaucophane host were always obtained from regions between cummingtonite lamellae. Representative AEM analyses of the glaucophane are presented in Tables 2 and 3. In contrast to cummingtonite, glaucophane generally contains at least some Fe^{3+} (Hawthorne, 1981, 1983). Studies of sodic amphiboles from blueschist-facies amphibolites by Miyashiro (1957), Borg (1967), Coleman and Papike (1968), and Wood (1980) have shown that there is complete miscibility between glaucophane and magnesioriebeckite, with Fe^{3+} readily substituting for Al in the M2 site. Optical examination of the sodic amphiboles showed that many of the grains have dark blue cores, which probably is caused by increased Fe^{3+} content (Bancroft and Burns, 1969). Furthermore, during the exsolution process, we would expect little or no Fe^{3+} to be partitioned into the cummingtonite structure, so that any Fe^{3+} present will be concentrated in the glaucophane. Although discussions by Hawthorne (1983) have indicated that determination of Fe^{3+} content by various normalization schemes usually yields meaningless results, an estimation of Fe^{3+} was made based on stoichiometric considerations for comparison purposes with previously reported pairs of sodic-ferromagnesian amphiboles.

The different recalculation methods used for the glaucophane analyses were carried out (1) assuming that all Fe is present as FeO and normalizing to 23 O atoms (Table 2), and (2) following the method of Laird and Albee (1981a), which involves a 23–O atom basis and normalization to fixed numbers of cations (Table 3). Normalization to 13 cations excluding Ca, Na, and K yielded

TABLE 2. Representative AEM analyses for glaucophane host

Amphibole formula: based on normalization to 23 O atoms and assuming all Fe as FeO									
Sample no.		VEB1-D	VEB1-D	VEB1-D	VEB1-B	VEB1-A	VEB1-D	VEB1-D	VEB1-E
Spectrum no.		EDG12B	EDG15B	EDG17B	EBG1B	EAG13B	EDG8B	EDG9B	EBE10B
Tetrahedral	Si	7.98	7.95	7.99	7.99	7.97	7.88	7.95	7.90
	Al	0.02	0.05	0.01	0.01	0.03	0.12	0.05	0.10
	Total T-site	8.00	8.00	8.00	8.00	8.00	8.00	8.00	8.00
Octahedral	Al	1.66	1.64	1.64	1.38	1.72	1.64	1.57	1.57
M1, M2, M3	Ti	0.00	0.01	0.00	0.01	0.00	0.00	0.01	0.01
	Cr	0.00	0.00	0.00	0.01	0.00	0.00	0.01	0.00
	Mg	2.20	2.16	2.21	2.44	2.19	2.36	2.29	2.29
	Fe^{2+}	1.13	1.19	1.15	1.16	1.08	1.00	1.12	1.12
	Total M1–M3	4.99	5.00	5.00	5.00	4.99	5.00	5.00	4.99
Octahedral	Ca	0.09	0.09	0.06	0.22	0.08	0.08	0.08	0.08
M4	Na	1.71	1.63	1.74	1.73	1.73	1.59	1.68	1.80
	Fe^{2+}	0.20	0.28	0.21	0.04	0.18	0.33	0.24	0.11
	Mn	0.00	0.00	0.00	0.01	0.00	0.00	0.00	0.00
	Total M4	2.00	2.00	2.01	2.00	1.99	2.00	2.00	1.99
A site	Na	0.06	0.02	0.11	0.33	0.04	0.07	0.12	0.28
	K	0.01	0.00	0.00	0.01	0.00	0.00	0.01	0.03
	Total A site	0.07	0.02	0.11	0.34	0.04	0.07	0.13	0.31
$Mg/(Mg + Fe^{2+})$		0.624	0.596	0.619	0.669	0.634	0.641	0.628	0.649

acceptable results in only a few cases where $(Ca + {}^{M4}Na) > 2.0$. This normalization prevents the appearance of any cummingtonite component in the amphibole formula, which may be present in this system. For the vast majority of analyses, normalization to 15 cations excluding K yielded acceptable results. The normalization scheme for each analysis is indicated in Table 3. The ratio of $Mg/(Mg + Fe^{2+})$ in the glaucophane ranged from 0.596 to 0.669 with an average value of 0.632 for the compositions shown in Table 2, and from 0.607 to 0.735 with an average value of 0.678 for the compositions shown in Table 3. The analyses indicated a small amount of Ca and low A-site occupancy. Comparison of the compositions given in Tables 2 and 3 indicates that the primary effects of normalization to fixed numbers of cations are (1) reduction of A-site occupancy, (2) decrease in both cummingtonite component (^{M4}Fe) and $^{[6]}Al$, and (3) increase of Na in the M4 site.

The sodic-ferromagnesian miscibility gap

The principles of amphibole crystal chemistry indicate that the compositional gap between sodic and ferromagnesian amphiboles is defined primarily by discontinuities in the M2 and M4 crystallographic sites (Robinson et al., 1982). By comparing the cummingtonite and glaucophane compositions (Tables 1, 2, and 3), it is evident that the exsolution process between cummingtonite and glaucophane obeys these principles, and that the cation exchange can be ideally expressed as $[^{M4}Na,^{M2}(Al,Fe^{3+})] = [^{M4}(Fe^{2+},Mg),^{M2}(Mg,Fe^{2+})]$. The average ratio of $Mg/(Mg + Fe^{2+})$ is slightly higher in the glaucophane (0.632 or 0.678) than in the cummingtonite (0.589), suggesting that slightly more Fe^{2+} is partitioned into the cummingtonite. In addition, although the bulk composition appears to be low in Ca, what Ca there is seems to be preferentially partitioned into the cummingtonite as is any Mn. The

TABLE 3. Representative AEM analyses for glaucophane host

Amphibole formula: 23 O atom basis with cations normalized to (1) 15 cations excluding K or (2) 13 cations excluding CNK									
Sample no.		VEB1-D	VEB1-D	VEB1-D	VEB1-B	VEB1-A	VEB1-D	VEB1-D	VEB1-E
Spectrum no.		EDG12B	EDG15B	EDG17B	EBG1B	EAG13B	EDG8B	EDG9B	EBE10B
Norm method		1	1	1	2	1	1	1	2
Tetrahedral	Si	7.94	7.94	7.93	7.96	7.94	7.84	7.88	7.83
	Al	0.06	0.06	0.07	0.04	0.06	0.16	0.12	0.17
	Total T-site	8.00	8.00	8.00	8.00	8.00	8.00	8.00	8.00
Octahedral	Al	1.62	1.62	1.57	1.34	1.70	1.60	1.50	1.49
M1, M2, M3	Ti	0.00	0.01	0.00	0.01	0.00	0.00	0.01	0.01
	Cr	0.00	0.00	0.00	0.01	0.00	0.00	0.01	0.00
	Fe^{3+}	0.20	0.07	0.32	0.19	0.13	0.20	0.37	0.41
	Mg	2.20	2.16	2.19	2.43	2.19	2.35	2.27	2.27
	Fe^{2+}	0.98	1.14	0.91	1.02	0.98	0.84	0.84	0.82
	Mn	0.00	0.00	0.00	0.01	0.00	0.00	0.00	0.00
	Total M1-M3	5.00	5.00	4.99	5.01	5.00	4.99	5.00	5.00
Octahedral	Ca	0.09	0.09	0.06	0.22	0.08	0.08	0.08	0.08
M4	Na	1.77	1.65	1.83	1.78	1.77	1.65	1.79	1.92
	Fe^{2+}	0.14	0.26	0.11	0.00	0.14	0.27	0.13	0.00
	Total M4	2.00	2.00	2.00	2.00	1.99	2.00	2.00	2.00
A site	Na	0.00	0.00	0.00	0.25	0.00	0.00	0.00	0.14
	K	0.01	0.00	0.00	0.01	0.00	0.00	0.01	0.03
	Total A site	0.01	0.00	0.00	0.26	0.00	0.00	0.01	0.17
$Mg/(Mg + Fe^{2+})$		0.661	0.607	0.681	0.705	0.659	0.679	0.700	0.735

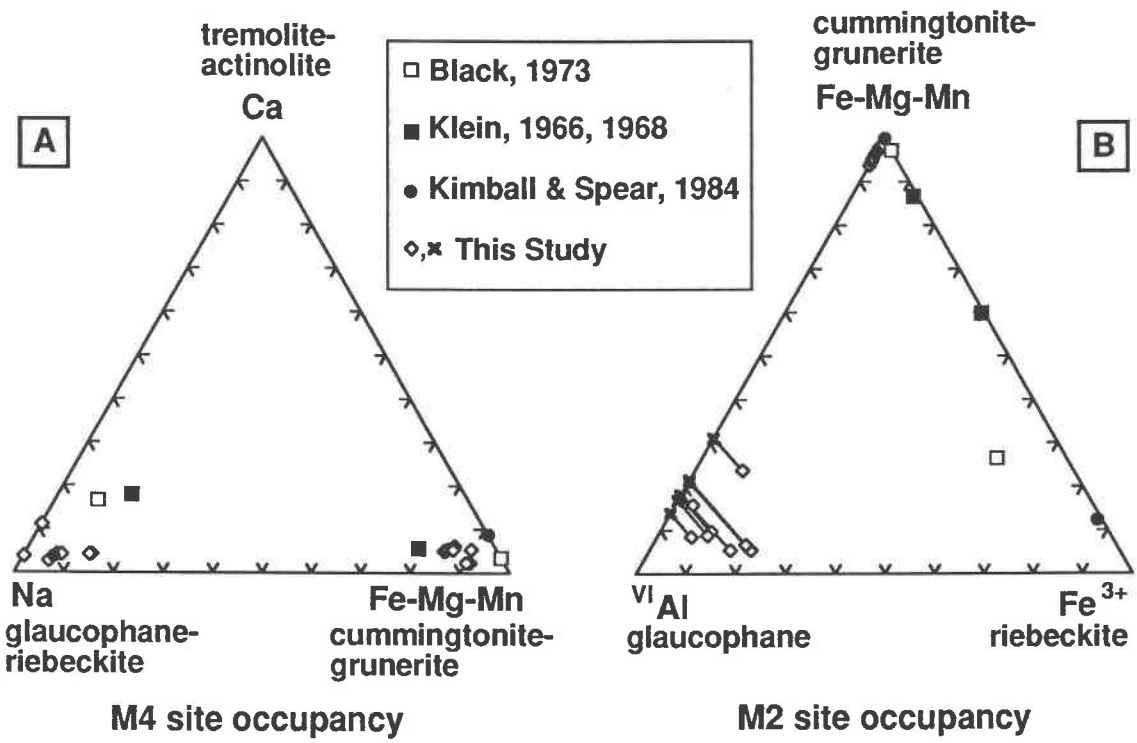

Fig. 6. Ternary composition diagrams showing M4 and M2 site occupancies for coexisting sodic-ferromagnesian amphibole inferred from chemical analyses. Symbols are as indicated. (**A**) M4 site occupancies. To maintain clarity, only the glaucophane compositions from Table 3 are plotted. These pairs clearly show the miscibility gap between sodic and ferromagnesian amphiboles. (**B**) M2 site occupancies. The base of the diagram is the solid-solution series between glaucophane and riebeckite. Both sets of glaucophane analyses (Tables 2 and 3) are plotted here with corresponding analyses connected by tie lines. Again, the miscibility gap between sodic and ferromagnesian amphiboles is clearly shown, as well as the large compositional difference between the sodic amphiboles in the present pair and those in the previously reported pairs.

partitioning of Ca into the cummingtonite structure is somewhat counterintuitive, based on cation size considerations for M4 in the respective structures. Indeed, coexisting amphibole pairs of Klein (1966, 1968) and Black (1973) show preferential Ca partitioning into the sodic amphibole; these minerals, however, are very Al poor. In the present case, Ca may favor cummingtonite over glaucophane partially because of charge imbalance resulting from divalent Ca ions (in M4) surrounded by trivalent Al ions in the M2 sites of glaucophane. In addition, Hawthorne (1983) indicates that mean ⟨M4-O⟩ bond lengths are strongly influenced by the cations in M1, M2, and M3, particularly M2 and that an increase in the size of the octahedral strip should lead to an increase in the mean ⟨M4-O(br)⟩ bond lengths. Examination of mean ionic radii in M1, M2, and M3 of the present pair indicate a significant increase in the cummingtonite. These, and other subtle effects, may also be important in the partitioning of Ca between cummingtonite and glaucophane.

It is also noteworthy that the compositions of both the cummingtonite and glaucophane varied little with precipitate size, suggesting that both limbs of the glaucophane-cummingtonite solvus are steep at these P-T conditions.

As mentioned earlier, several other pairs of coexisting sodic-ferromagnesian amphiboles have been reported in the literature. Klein (1966, 1968), Black (1973), and Kimball and Spear (1984) describe cummingtonite or grunerite coexisting with riebeckite, whereas Ghose et al. (1974) and Shau et al. (1989) report fine-scale exsolution textures involving compositionally complex Mn-rich amphiboles from the Mn mines at Tirodi, Maharashtra, India. These two unusual amphiboles have intermediate compositions between magnesio-arfvedsonite and magnesio-riebeckite and manganoan cummingtonite and richterite, respectively (Shau et al., 1989).

Since the M4 and M2 sites play a critical role in this exsolution process, the previously reported pairs (with the exception of the Mn-rich amphiboles from India) and the present pairs of compositions are compared on ternary diagrams showing these site occupancies (Fig. 6).

Figure 6A shows the idealized occupancy of the M4 site, which was allocated using the following cation ordering sequence: Na ≈ Ca ≥ Fe^{2+} ≥ Mn > Mg (Hawthorne, 1983). Because the difference in computed M4 site occupancy for compositions in Tables 2 and 3 is small, only glaucophane compositions from Table 3 have been

plotted. From this diagram, the miscibility gap between sodic and ferromagnesian amphiboles is clearly shown. Since on this diagram glaucophane and riebeckite plot at the same apex, the distinction between the present pair and previously reported pairs is not evident. This distinction, however, becomes clear by comparing the sodic amphibole compositions shown in Tables 2 and 3, which indicate a high Al content, with the Al-poor riebeckite compositions reported by previous authors. This difference is further illustrated in Figure 6B, which shows the idealized contents of the M2 site for the different studies. Several cation species may occupy the M2 site, but X-ray diffraction and Mössbauer spectroscopy studies suggest the following cation preference for M2: $Al \approx Fe^{3+} > Ti > Mg > Fe^{2+}$ (Hawthorne, 1983). The occupancy of M2 was apportioned using this sequence. Glaucophane analyses from both Tables 2 and 3 are plotted in Figure 6B, with corresponding analyses connected by tie lines. The base of this diagram represents the solid solution series between glaucophane and riebeckite. Again, the miscibility gap between sodic and ferromagnesian amphiboles is clearly shown. These combined data suggest that the miscibility gap between sodic and ferromagnesian amphiboles is continuous across the entire solid solution series between glaucophane and riebeckite, with the glaucophane end of the solvus having the steeper limbs. The present results also show that the eclogites from northern Vermont contain the first evidence of equilibrium coexistence of normal low-Fe glaucophane and cummingtonite.

Orientation of the exsolution lamellae

For the following discussion, all lamellar orientations will be described in terms of the $C2/m$ unit-cell setting for the monoclinic amphiboles. The relationships between the $C2/m$ cell setting and the $I2/m$ cell setting are discussed fully by Whittaker and Zussman (1961), Jaffe et al. (1968), and Thompson (1978).

Numerous studies of exsolved monoclinic amphiboles using a variety of techniques (e.g., Vernon, 1962; Ross et al., 1968; Jaffe et al., 1968; Robinson et al., 1969, 1971b; Ross et al., 1969; Spear, 1982; Gittos et al., 1974, 1976) have indicated that the lamellae are most commonly oriented nearly parallel to the $(\bar{1}01)$ and (100) planes of the host. These irrational phase boundaries may be termed "optimal phase boundaries" (terminology of Bollman and Nissen, 1968) and are designated "$\bar{1}01$" and "100" (in the $I2/m$ setting, "$\bar{1}01$" becomes "001"). These boundaries represent planes of dimensional best fit between the two amphibole lattices, achieved by slight rotation of the lattices with respect to each other (Robinson et al., 1971b, 1977). Robinson et al. (1977) have termed this type of rotation "phase-boundary lattice rotation." They have also shown in many cases the phase boundaries are "much better than optimal . . . because their orientation permits an exact lattice match at the two-phase interface" (Robinson et al., 1977), hence the term "exact phase boundary." The exact orientations of optimal phase boundaries or exact phase boundaries depend on several factors, the dominant one being the magnitude of the dimensional (or structural) misfit between the two crystal lattices (Cahn, 1968; Bollman and Nissen, 1968; Robinson et al., 1971b, 1977; Willaime and Brown, 1974; Fleet et al., 1980; Fleet, 1982). In the present amphibole pair, the cummingtonite lamellae are in a significantly different orientation from those previously reported for clinoamphiboles that are not constrained by the "exact phase-boundary theory" of Robinson et al. (1971b, 1977).

The orientation of the lamellae was determined using a combination of selected-area electron diffraction patterns and conventional (CTEM) and high-resolution (HRTEM) images. Figures 1, 2, and 5A are low-magnification TEM images showing the exsolution lamellae viewed nearly edge-on with the plane of the discs perpendicular to the plane of the figures. Note the sharp interfaces between the host and the lamellae. When the sample is tilted out of this orientation, the interface becomes poorly defined and shows displacement-fringe contrast.

The SAED pattern for the edge-on orientation is illustrated in Figure 5B. The electron beam is parallel to the [102] zone axis of the host, showing the $\mathbf{b}^*$-$[20\bar{1}]^*$ reciprocal lattice plane. By comparing the SAED pattern with its corresponding image, it is evident that the **b** axis, which is parallel to $\mathbf{b}^*$, bisects the obtuse angle made by the intersecting lamellae. Therefore, the two sets of lamellae are symmetrically related by the mirror plane perpendicular to **b**. One important property of the reciprocal lattice is that any vector in reciprocal space, $\mathbf{r}^*_{hkl}$, is perpendicular to the real space planes with the same indices, (hkl) (e.g., Hirsch et al., 1977, p. 93). Using this relationship, we found the $[28\bar{1}]^*$ and $[2\bar{8}\bar{1}]^*$ reciprocal lattice vectors to be nearly perpendicular to the two sets of lamellae (see Fig. 5). This means that the exsolution lamellae are oriented nearly parallel to the $(28\bar{1})$ and $(2\bar{8}\bar{1})$ planes of the host and are designated "$28\bar{1}$" and "$2\bar{8}\bar{1}$." This unusual orientation is quite different from that of the common "$\bar{1}01$" and "100" clinoamphibole exsolution lamellae.

These relationships are diagrammed in Figure 7, which schematically shows several important orientations in clinoamphiboles. The diagram shows {110} cleavage faces and the (010) plane (lightly stippled). Contained within the (010) plane are traces of a series of common "$\bar{1}01$" and "100" lamellae (cf. Jaffe et al., 1968, Fig. 2, p. 777), which are seen in cross section when viewed down **b**. Also shown is one pair of lamellae in the new orientation (darkly stippled). The line of intersection of the two lamellae is near the [102] zone and is contained in the **a**–**c** plane. From this figure, the symmetrical relationship between the "$28\bar{1}$" and "$2\bar{8}\bar{1}$" lamellae can also be seen.

More insight into this unusual orientation can be gained by careful examination of SAED patterns. Figure 8 illustrates exsolved glaucophane viewed down the **c** axis. The TEM image (Fig. 8A) shows the cummingtonite lamellae, and the corresponding SAED pattern (Fig. 8B) contains the $\mathbf{a}^*$-$\mathbf{b}^*$ reciprocal lattice plane. Careful examination of

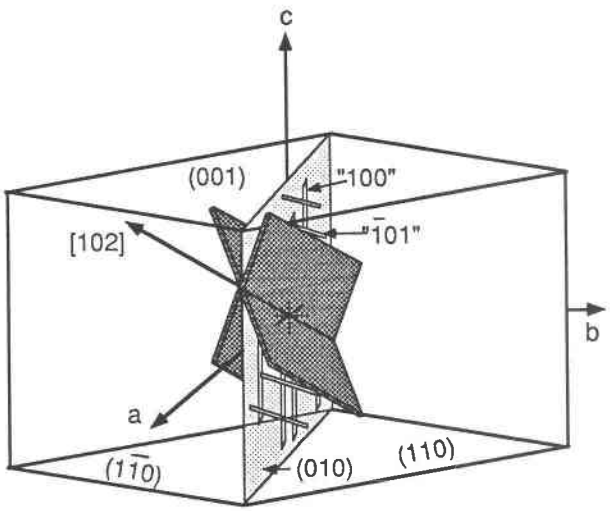

Fig. 7. Schematic diagram showing several important orientations in monoclinic $C2/m$ amphibole. The figure is bounded by {110} cleavage faces. The (010) plane is shown in a light stippled pattern. Typical "$\bar{1}$01" and "100" clinoamphibole exsolution lamellae would be viewed in sections normal to **b**. A set of these lamellae is shown sketched in cross section in the (010) plane. Also shown is a pair of lamellae in the new orientation (darker stipple). The line formed by the intersection of the lamellae is the [102] zone. The symmetrical relationships between the "28$\bar{1}$" and "2$\bar{8}\bar{1}$" orientations can also be seen in this figure.

this pattern and the pattern in Figure 5B reveals distinct splitting of the diffraction spots caused by the presence of two phases. Note that both sets of lamellae, the "28$\bar{1}$" and "2$\bar{8}\bar{1}$" sets, produce an extra spot around a main glaucophane reflection, resulting in a three-spot pattern resembling rabbit ears (see insets, Figs. 5B and 8B). Note that the spots caused by the lamellae are not round, but elongated. This is because lamellae are very thin and produce a spike-shaped intensity distribution in reciprocal space, caused by the shape effect (see Hirsch et al., 1977, p. 98). The long dimension of each reciprocal-lattice spike is parallel to the thin direction of the lamellae creating it (e.g., in the inset of Fig. 5B, the left rabbit ear is formed by the "28$\bar{1}$" lamellae and the right rabbit ear by the "2$\bar{8}\bar{1}$" lamellae). In addition to the rabbit ears, it is evident from Figures 5B and 8B that the degree of spot splitting is greater parallel to **b*** than parallel to [20$\bar{1}$]* or **a***. This indicates that the major difference in lattice parameters between the cummingtonite and glaucophane is in the **b** dimension.

For lamellar precipitates to obey the "exact phase-boundary theory" of Robinson et al. (1971b, 1977), the two related lattices are constrained to have identical b-axis lengths. When this is the case, the planes of dimensional best fit between the two lattices will be near ($\bar{1}$01) and (100). Since the coexisting cummingtonite and glaucophane possess substantially different b-axis lengths, it is not surprising to find a different optimal phase boundary orientation for this pair. A similar case exists for coexisting anthophyllite-gedrite, in which the differing b axes result in exsolution lamellae nearly parallel to (010) and (120) (Robinson et al., 1969; Christie and Olsen, 1974; Gittos et al., 1976; Spear, 1980). Optimal phase boundary calculations were performed to see if the unusual orientation of the cummingtonite lamellae could be rationalized in terms of optimal phase boundary theory.

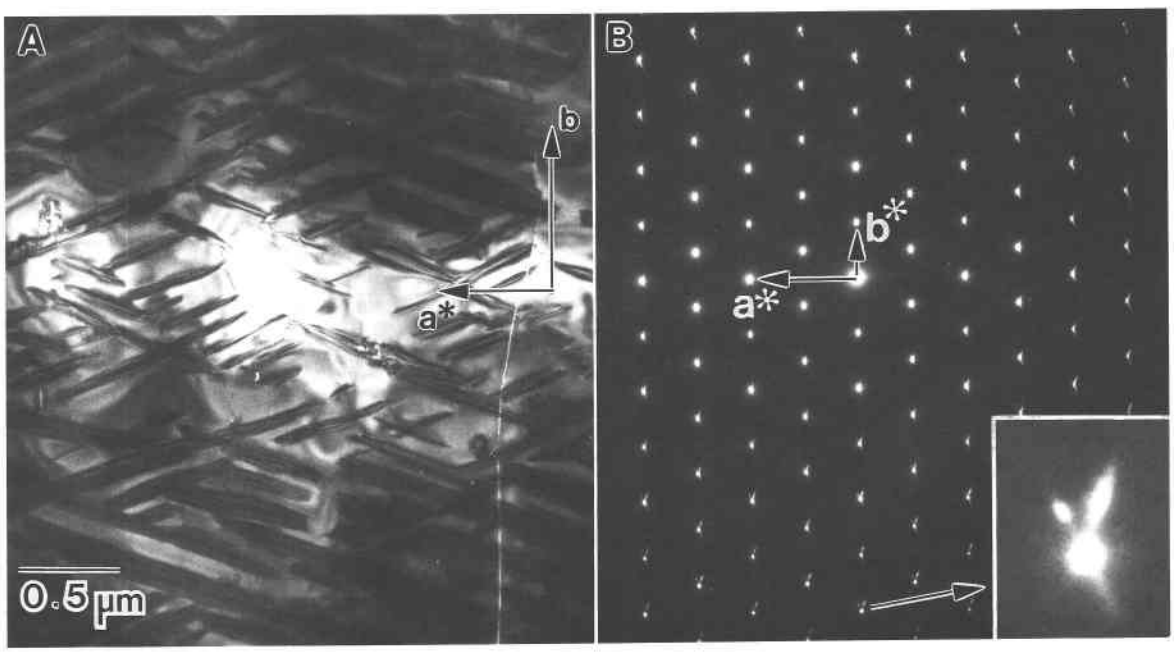

Fig. 8. (**A**) TEM image of exsolved glaucophane viewed down the **c** axis. The cummingtonite lamellae show displacement-fringe contrast. (**B**) Corresponding SAED pattern showing the **a***-**b*** reciprocal lattice plane. Note the pronounced splitting of the diffraction spots in the **b*** direction, giving the distinctive "rabbit ear" appearance (inset).

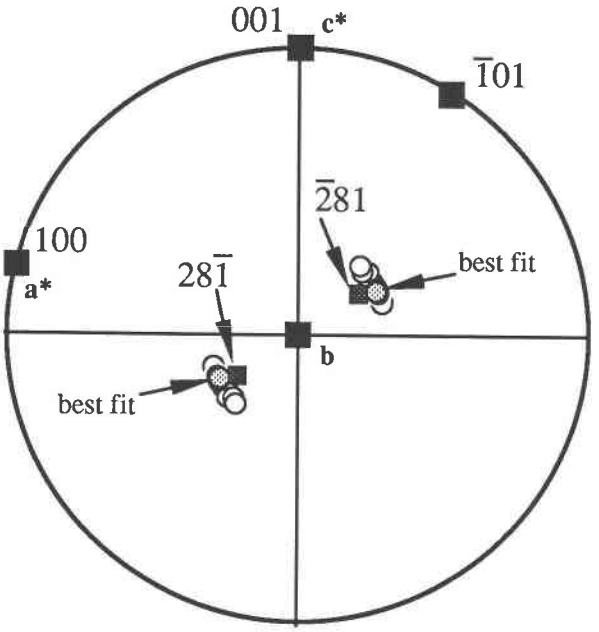

Fig. 9. Stereographic projection down **b** of glaucophane onto the **a***-**c*** reciprocal lattice plane. Poles for calculated and observed optimal phase boundary planes are shown as follows. The stippled squares indicate the poles for $(28\bar{1})$ and $(\bar{2}81)$, the observed orientations. Note that symmetrically related poles $(2\bar{8}\bar{1})$ and $(\bar{2}\bar{8}1)$ project in the lower hemisphere. The stippled circles indicate the poles for the calculated planes of best dimensional fit (optimal phase boundary) between unstrained glaucophane and cummingtonite lattices. The angular difference between the poles for observed and calculated optimal phase boundaries is less than 5°. The open circles are poles for calculated optimal phase boundaries within 1.0% relative misfit between the lattices.

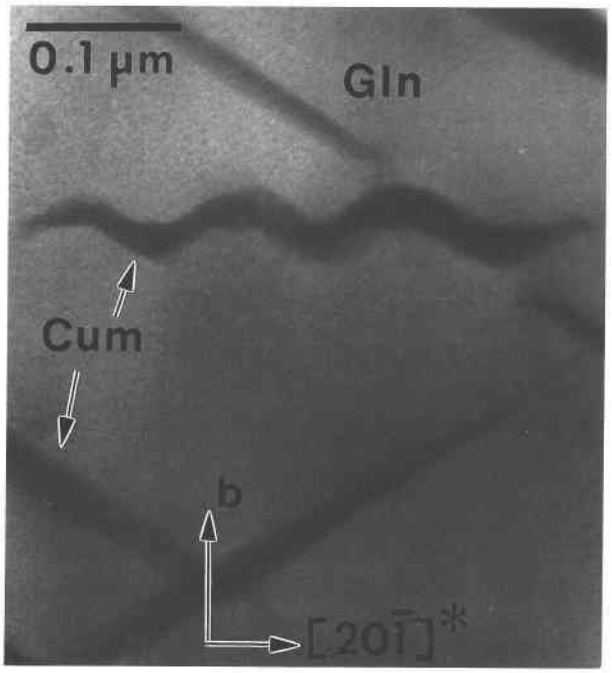

Fig. 10. TEM image of exsolved glaucophane consistent with heterogeneous nucleation of cummingtonite on a dislocation. Note the regular alternation of the "$28\bar{1}$" and "$2\bar{8}\bar{1}$" orientations along the dislocation. This pattern probably developed because of the symmetrical relationship between the two lamellar orientations. During growth, it was energetically more favorable for the lamella to switch orientations and maintain close proximity to the dislocation rather than proceed further out into nondefective material. The electron beam is parallel to [102].

Optimal phase boundary calculations

The dimensional misfit and orientations of the optimal phase boundaries between intergrown cummingtonite-glaucophane were determined using the three-dimensional lattice-fitting program (EPLAG) of Fleet (1982, 1984). This version of EPLAG calculates only the area misfit between normalized equivalent (*hkl*) planes in the two related lattices and makes no estimate of elastic strain energy. The area strain was calculated at grid points on a hemisphere about the **b** axis using a grid interval of 1°. Each grid point corresponds to a stereographic pole of an interatomic plane, (*hkl*), and is described in terms of the spherical coordinates (D, E), where D is a counterclockwise rotation around **b** and E is a clockwise rotation around an axis normal to **b** (see Fleet, 1982, for details of the 3-D theory). The results may then be displayed on a stereographic projection down **b**, the equatorial plane being the **a***-**c*** reciprocal lattice plane.

The EPLAG program predicts optimal phase boundaries based on unstrained lattice parameters for the two phases. Since both amphiboles are monoclinic with $C2/m$ space group symmetry, no modification of either lattice was necessary (cf. Fleet et al., 1980; Fleet and Arima, 1985). Because lattice parameter determination using SAED patterns gives rise to relatively inaccurate values, an independent means was used to obtain lattice parameters for the cummingtonite and glaucophane.

Glaucophane crystals were hand picked from the eclogite and crushed for X-ray powder diffraction. The X-ray powder data were obtained using a Scintag automated X-ray powder diffractometer. The mineral separate also contained quartz, which served as an internal standard. Following the method of Post and Bish (1988), a Rietveld refinement of the data set was performed using as a model structure the results of a single-crystal refinement of Papike and Clark (1968). The refinement yielded the following parameters for the glaucophane: a = 0.9536(4) nm, b = 1.7753(7) nm, c = 0.5305(2) nm, α = 90.0°, β = 103.58(3)°, γ = 90.0°.

Because of the small amount and size of cummingtonite lamellae present, it was impossible to determine unstrained lattice parameters for the cummingtonite directly. Studies have shown, however, that there is nearly a linear relationship between unit-cell parameters and composition of ferromagnesian amphiboles in the cummingtonite-grunerite series (Klein, 1964; Viswanathan and Ghose, 1965; Klein and Waldbaum, 1967). Using the re-

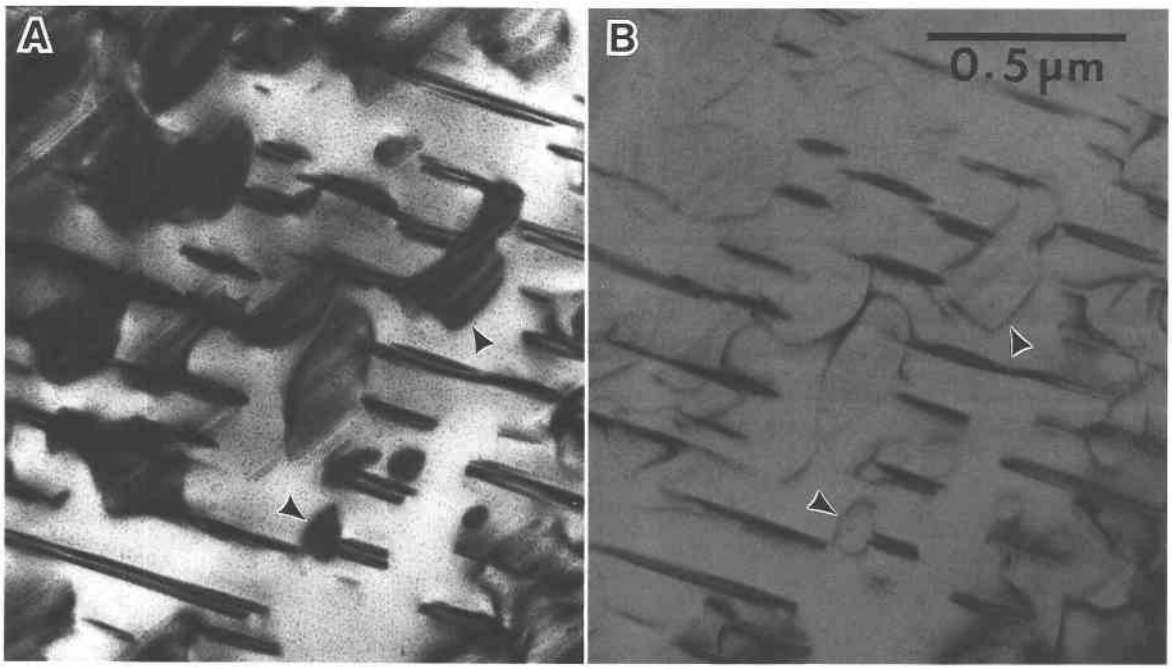

Fig. 11. TEM image of fine-scale cummingtonite lamellae in glaucophane. (**A**) In this orientation one set of lamellae is tilted with respect to the electron beam and shows pronounced displacement-fringe contrast. Note that the cummingtonite lamellae start out as small pancake-shaped discs (arrows). (**B**) The same area is tilted further to eliminate displacement-fringe contrast. Note that the outer boundaries of the small pancake-shaped lamellae are still visible and resemble dislocation loops. This contrast is due to coherency strain, which is maximized at the edges of the thin lamellae. The smallest lamellae are fully contained in the thin foil.

gression equations of Viswanathan and Ghose (1965), unstrained lattice parameters were calculated using the average cummingtonite composition, determined from AEM, with $Mg/(Mg + Fe^{2+})$ equal to 0.589. The resultant unit cell is $a = 0.95196$ nm, $b = 1.81475$ nm, $c = 0.53146$ nm, $\alpha = 90.0°$, $\beta = 102.142°$, $\gamma = 90.0°$.

The results of the optimal phase boundary calculations obtained using this set of lattice parameters are presented in a stereographic projection down **b** (Fig. 9). Note that all the calculated minima (stippled circles, open circles) plot within a few degrees of the poles for $(28\bar{1})$ and $(\bar{2}81)$ (stippled squares in Fig. 9). Thus, these results agree well with the observed lamellar orientations and indicate that the dimensional misfit between the glaucophane and cummingtonite lattices is the dominant factor controlling the lamellar orientations, with the optimal phase boundaries being irrational planes near $(28\bar{1})$ and $(2\bar{8}\bar{1})$.

Exsolution mechanisms

The exsolution microstructures observed in these glaucophane samples suggest that both heterogeneous and homogeneous nucleation of cummingtonite occurred during cooling.

All of the lamellae are coherently intergrown with the host (Fig. 3), and HRTEM images have not revealed any defects associated with growth ledges like those observed in some exsolved pyroxenes (Champness and Lorimer, 1973; Kohlstedt and Vander Sande, 1976) or other monoclinic amphiboles (Gittos et al., 1974). Heterogeneous nucleation of lamellae on dislocations has been observed (Fig. 10), but most of the lamellae have no structural defects associated with them (Figs. 1, 2, and 5) and are totally enclosed within the host. Figure 11 shows an area that has developed very fine-scale lamellae. In Figure 11A, one set of lamellae is tilted with respect to the electron beam and shows pronounced displacement-fringe contrast. Note that in some cases, indicated by arrows, the three-dimensional shape of the lamellae is revealed as being tiny discs. In Figure 11B, the same area has been tilted slightly to show different contrast. In this image, the edges of the tilted lamellae are well defined by dark lines of contrast that closely resemble the appearance of dislocation loops (Hirsch et al., 1977). This contrast is due to coherency strain between the glaucophane and cummingtonite lattices, which is maximized at the edges of the lamellae. This coherency-strain contrast can also be seen in the larger lamellae, maximized at the lamellar tips (Figs. 2 and 5).

These observations suggest that perhaps the majority of the lamellae nucleated homogeneously and may represent coarsening of early GP zones. It is also possible, but unlikely, that some of these lamellae nucleated heterogeneously on dislocations that were somehow obliterated as the lamellae grew. As mentioned earlier, in a few instances, tiny homogeneously distributed platelets or GP zones have developed between larger lamellae (Fig.

4). These are mostly likely the result of homogeneous nucleation in areas that have become supersaturated in cummingtonite component at temperatures below the main precipitation event. Similar GP zones have been observed in calcic amphibole (Gittos et al., 1974) and orthoamphiboles (Gittos et al., 1976).

In some glaucophane there are regions with very few or no lamellae present. The composition of the glaucophane in these areas is essentially the same as the host composition between lamellae in the exsolved areas. In addition, the highest precipitate density generally occurs in the cores of the grains. These observations, combined with optical observations, suggest that the glaucophane shows primary chemical zoning with Fe-Mg-enriched cores and that the range of bulk glaucophane compositions straddles the glaucophane limb of the glaucophane-cummingtonite solvus. This chemical zoning led to regions of different precipitate concentration. We also observed that the unexsolved areas commonly have a higher dislocation density than the exsolved areas. This might be considered evidence for heterogeneous nucleation on dislocations which were subsequentially destroyed as the lamellae coarsened, as mentioned above, but more likely suggests that the presence of exsolution lamellae blocked the formation and propagation of dislocations in these areas during deformation.

All the cummingtonite lamellae have the same orientation, regardless of precipitate size or mechanism of formation. This observation and the optimal phase boundary calculations suggest that "$28\bar{1}$" and "$2\bar{8}\bar{1}$" are the stable orientations for the optimal phase boundaries over a range of temperature, with the primary crystallographic control being the different b-axis lengths.

Conclusions

The TEM-AEM study of glaucophane samples from eclogitic assemblages from northern Vermont has yielded important new information with regard to the crystal chemistry and crystallography of coexisting sodic and ferromagnesian amphiboles. These results represent the first finding of exsolution in the high-pressure/low-temperature amphiboles characteristic of blueschists and eclogites. The present results combined with previously reported data suggest that the miscibility gap between sodic and ferromagnesian amphiboles is continuous across the glaucophane-riebeckite solid solution series, with the glaucophane end of the solvus having a steeper limb.

The cummingtonite exsolution lamellae are submicroscopic, reaching a maximum thickness of about 60 nm. The predominant exsolution process appears to be one of homogeneous nucleation and growth in which the lamellae start out as tiny pancake-shaped discs, which coarsen homogeneously in two dimensions. Evidence for heterogeneous nucleation has been observed but is apparently not the dominant process in these samples. Tiny, homogeneously distributed platelets (GP zones) of cummingtonite have been observed in areas between coarse lamellae in one sample.

The orientation of the cummingtonite lamellae represents a new orientation for exsolution lamellae in clinoamphiboles that is significantly different from all previously reported lamellar orientations (typically "$\bar{1}01$" and "100"). Analysis has shown that the lamellae are coherent, with lamellar-host interfaces being irrational planes nearly parallel to $(28\bar{1})$ and $(2\bar{8}\bar{1})$ of the host. These two orientations are symmetrically related by the mirror plane normal to **b**. Three-dimensional optimal phase boundary calculations for intergrown glaucophane-cummingtonite using unstrained lattice parameters have shown that the observed lamellar-host interfaces represent planes of best dimensional fit between the glaucophane and cummingtonite lattices. This result is consistent with previous work showing lattice misfit as being the dominant controlling factor for lamellar orientations in chain silicates.

Acknowledgments

Special thanks go to Jo Laird for discussions about the rocks from the Tillotson Peak area and for leading one of us (E.A.S.) to the concealed Eclogite Brook locality. Jeff Post contributed his expertise for the Rietveld refinement of the glaucophane, which is greatly appreciated. Thanks also go to Michael Fleet for the EPLAG program. Charles Burnham and Malcolm Ross provided thorough reviews of the manuscript, which we greatly appreciate. This work benefited substantially from discussions with Peter Heaney, George Guthrie, Ken Livi, and Jill Banfield. The electron microscopy was carried out at The Johns Hopkins TEM Facility (established with NSF grant EAR-8300365) under support from NSF grants EAR-8609277 and EAR-8903630.

References cited

Bancroft, G.M., and Burns, R.G. (1969) Mössbauer and absorption spectral study of alkali amphiboles. Mineralogical Society of America Special Paper 2, 137–148.

Bancroft, G.M., Burns, R.G., and Maddock, A.G. (1967a) Determination of the cation distribution in the cummingtonite-grunerite series by Mössbauer spectroscopy. American Mineralogist, 52, 1009–1026.

Bancroft, G.M., Maddock, A.G., and Burns, R.G. (1967b) Applications of the Mössbauer effect to silicate mineralogy—I. Iron silicates of known crystal structure. Geochimica et Cosmochimica Acta, 31, 2219–2246.

Black, P.M. (1973) Mineralogy of New Caledonian metamorphic rocks II. Amphiboles from the Ouégoa District. Contributions to Mineralogy and Petrology, 39, 55–64.

Bollman W., and Nissen, H.-U. (1968) A study of optimal phase boundaries: The case of exsolved feldspars. Acta Crystallographica, A24, 546–557.

Borg, I.Y. (1967) Optical properties and cell parameters in the glaucophane-riebeckite series. Contributions to Mineralogy and Petrology, 15, 67–92.

Bothner, W.A., and Laird, J. (1987) Structure and metamorphism at Tillotson Peak, North-Central Vermont. In D.S. Westerman, Ed., Guidebook for field trips in Vermont, vol. 2, p. 383–405. 79th Annual Meeting of the New England Intercollegiate Geological Conference, Montpelier, Vermont.

Cahn, J.W. (1968) Spinodal decomposition. Transactions of the Metallurgical Society of AIME, 242, 166–180.

Champness, P.E., and Lorimer, G.W. (1973) Precipitation (exsolution) in an orthopyroxene. Journal of Materials Science, 8, 467–474.

Christie, O.H.J., and Olsen, A. (1974) Spinodal precipitation in minerals and some new observations. Bullétin de la Société Français de Minéralogie et Cristallographie, 97, 202–205.

Coleman, R.G., and Papike, J.J. (1968) Alkali amphiboles from the blueschists of Cazadero, California. Journal of Petrology, 9, 105–122.

Doll, C.G., Cady, W.M., Thompson, J.B., Jr., and Billings, M.P. (1961) Centennial geologic map of Vermont. Vermont Geologic Survey, Montpelier, Vermont.

Finger, L.W. (1969) The crystal structure and cation distribution of a grunerite. Mineralogical Society of America Special Paper 2, 95–100.

Fischer, K.F. (1966) A further refinement of the crystal structure of cummingtonite, $(Mg,Fe)_7(Si_4O_{11})OH)_2$. American Mineralogist, 51, 814–818.

Fleet, M.E. (1982) Orientation of phase and domain boundaries in crystalline solids. American Mineralogist, 67, 926–936.

——— (1984) Orientation of feldspar intergrowths: Application of lattice misfit theory to cryptoperthites and *e*-plagioclase. Bulletin de Minéralogie, 107, 509–519.

Fleet, M.E., and Arima, M. (1985) Oriented hematite inclusions in sillimanite. American Mineralogist, 70, 1232–1237.

Fleet, M.E., Bilcox, G.A., and Barnett, R.L. (1980) Oriented magnetite inclusions in pyroxenes from the Grenville Province. Canadian Mineralogist, 18, 89–99.

Ghose, S. (1961) The crystal structure of cummingtonite. Acta Crystallographica, 14, 622–627.

——— (1981) Subsolidus reactions and microstructures in amphiboles. In Mineralogical Society of America Reviews in Mineralogy, 9A, 325–372.

Ghose, S., Forbes, W.C., and Phakey, P.P. (1974) Unmixing of an alkali amphibole (tirodite) into magnesiorichterite and magnesioriebeckite. Indian Journal of Earth Sciences, 1, 37–42.

Gittos, M.F., Lorimer, G.W., and Champness, P.E. (1974) An electron-microscopic study of precipitation (exsolution) in an amphibole (the hornblende-grunerite system). Journal of Materials Science, 9, 184–192.

——— (1976) The phase distributions in some exsolved amphiboles. In H.-R. Wenk, P.E. Champness, J.M. Cristie, J.M. Cowley, A.H. Heuer, G. Thomas, and N.J. Tighe, Eds., Electron microscopy in mineralogy, p. 238–247. Springer-Verlag, Berlin.

Hafner, S.S., and Ghose, S. (1971) Iron and magnesium distribution in cummingtonites $(Fe,Mg)_7Si_8O_{22}(OH)_2$. Zeitschrift für Kristallographie, 133, 301–326.

Hawthorne, F.C. (1981) Crystal chemistry of the amphiboles. In Mineralogical Society of America Reviews in Mineralogy, 9A, 1–102.

——— (1983) The crystal chemistry of the amphiboles. Canadian Mineralogist, 21, 173–480.

Hirsch, P., Howie, A., Nicholson, R.B., Pashley, D.W., and Whelen, M.J. (1977) Electron microscopy of thin crystals, 563 p. Krieger Publishing, Malabar, Florida.

Jaffe, H.W., Robinson, P., and Klein, C. (1968) Exsolution lamellae and optic orientation of clinoamphiboles. Science, 160, 776–778.

Kimball, K.L., and Spear, F.S. (1984) Metamorphic petrology of the Jackson County Iron Formation, Wisconsin. Canadian Mineralogist, 22, 605–619.

Kitamura, M. (1981) Morphology change of exsolution lamellae of pigeonite in Bushveld augite—An electron microscopic observation. Proceedings of the Japan Academy, Series B, 57, 183–187.

Klein, C., Jr. (1964) Cummingtonite-grunerite series: A chemical, optical and X-ray study. American Mineralogist, 49, 963–982.

——— (1966) Mineralogy and petrology of the metamorphosed Wabush iron formation, Southwestern Labrador. Journal of Petrology, 7, 246–305.

——— (1968) Coexisting amphiboles. Journal of Petrology, 9, 281–330.

Klein, C., Jr., and Waldbaum, D.R. (1967) X-ray crystallographic properties of the cummingtonite-grunerite series. Journal of Geology, 75, 379–392.

Kohlstedt, D.L., and Vander Sande, J.B. (1976) On the detailed structure of ledges in an augite-enstatite interface. In H.-R. Wenk, P.E. Champness, J.M. Christie, J.M. Cowley, A.H. Heuer, G. Thomas, and N.J. Tighe, Eds., Electron microscopy in mineralogy, p. 234–237. Springer-Verlag, Berlin.

Laird, J. (1977) Phase equilibria in mafic schist and the polymetamorphic history of Vermont. Ph.D. thesis, California Institute of Technology, Pasadena, California.

Laird, J., and Albee, A.L. (1981a) High-pressure metamorphism mafic schist from northern Vermont. American Journal of Science, 281, 97–126.

——— (1981b) Pressure, temperature, and time indicators in mafic schist: Their application to reconstructing the polymetamorphic history of Vermont. American Journal of Science, 281, 127–175.

Lanphere, M.A., and Albee, A.L. (1974) $^{40}Ar/^{39}Ar$ age measurements in the Worcester Mountains: Evidence of Ordovician and Devonian metamorphic events in northern Vermont. American Journal of Science, 274, 545–555.

Leake, B.E. (1978) Nomenclature of amphiboles. American Mineralogist, 63, 1023–1053.

Livi, K.J.T., and Veblen, D.R. (1987) "Eastonite" from Easton, Pennsylvania: A mixture of phlogopite and a new form of serpentine. American Mineralogist, 72, 113–125.

——— (1989) Transmission electron microscopy of interfaces and defects in intergrown pyroxenes. American Mineralogist, 74, 1070–1083.

Miyashiro, A. (1957) The chemistry, optics and genesis of the alkali amphiboles. Journal of the Faculty of Science, University of Tokyo, section II, 11, 57–83.

Nord, G.L., Jr., (1980) The composition, structure, and stability of Guinier-Preston zones in lunar and terrestrial orthopyroxene. Physics and Chemistry of Minerals, 6, 109–128.

Papike, J.J., and Clark, J.R. (1968) The crystal structure and cation distribution of glaucophane. American Mineralogist, 53, 1156–1173.

Post, J.E., and Bish, D.L. (1988) Rietveld refinement of the todorokite structure. American Mineralogist, 73, 861–869.

Rietmeijer, F.J.M., and Champness, P.E. (1982) Exsolution structures in calcic pyroxenes from the Bjerkreim-Sokndal lopolith, SW Norway. Mineralogical Magazine, 45, 11–24.

Robinson, P. (1963) Gneiss domes of the Orange Area, West Central Massachusetts and New Hampshire. Ph.D. dissertation, Harvard University, Cambridge, Massachusetts.

Robinson, P., and Jaffe, H. (1969) Chemographic exploration of amphibole assemblages from central Massachusetts and southwestern New Hampshire. Mineralogical Society of America Special Paper 2, 251–274.

Robinson, P., Jaffe, H., Klein, C., and Ross, M. (1969) Equilibrium coexistence of three amphiboles. Contributions to Mineralogy and Petrology, 22, 248–258.

Robinson, P., Ross, M., and Jaffe, H.W. (1971a) Composition of the anthophyllite-gedrite series, comparisons of gedrite-hornblende, and the anthophyllite-gedrite solvus. American Mineralogist, 56, 1005–1041.

Robinson, P., Jaffe, H.W., Ross, M., and Klein, C. (1971b) Orientations of exsolution lamellae in clinopyroxenes and clinoamphiboles: Consideration of optimal phase boundaries. American Mineralogist, 56, 909–939.

Robinson, P., Ross, M., Nord, G.L., Jr., Smyth, J.R., and Jaffe, H.W. (1977) Exsolution lamellae in augite and pigeonite: Fossil indicators of lattice parameters at high temperature and pressure. American Mineralogist, 62, 857–873.

Robinson, P., Spear, F.S., Schumacher, J.C., Laird, J. Klein, C., Evans, B.W., and Doolan, B. L. (1982) Phase relations of metamorphic amphiboles: Natural occurrence and theory. In Mineralogical Society of America Reviews in Mineralogy, 9B, 1–227.

Ross, M., Papike, J.J., and Weiblen, P.W. (1968) Exsolution in clinoamphiboles. Science, 159, 1099–1104.

Ross, M., Papike, J.J., and Shaw, K.W. (1969) Exsolution textures in amphiboles as indicators of subsolidus thermal histories. Mineralogical Society of America Special Paper 2, 275–299.

Shau, Y.-H., Peacor, D.R., Ghose, S., and Phakey, P.P. (1989) Transmission electron microscopic study of spinodal decomposition in Mn-bearing alkali amphiboles ("Tirodite") from India. Eos, 70, 353.

Smelik, E.A., and Veblen, D.R. (1989) A five-amphibole assemblage from blueschists in northern Vermont. American Mineralogist, 74, 960–965.

Spear, F. (1980) The gedrite-anthophyllite solvus and the composition limits of orthoamphibole from the Post Pond Volcanics, Vermont. American Mineralogist, 65, 1103–1118.

——— (1982) Phase equilibria of amphibolites from the Post Pond Volcanics, Mt. Cube Quadrangle, Vermont. Journal of Petrology, 23, 383–426.

Stout, J.H. (1970) Three-amphibole assemblages and their bearing on the anthophyllite-gedrite miscibility gap (abs.). American Mineralogist, 55, 312–313.

——— (1971) Four coexisting amphiboles from Telemark, Norway. American Mineralogist, 56, 212–224.
——— (1972) Phase petrology and mineral chemistry of coexisting amphiboles from Telemark, Norway. Journal of Petrology, 13, 99–146.
Thompson, J.B., Jr. (1978) Biopyriboles and polysomatic series. American Mineralogist, 63, 239–249.
Vernon, R.H. (1962) Coexisting cummingtonite and hornblende in amphibolite from Duchess, Queensland, Australia. American Mineralogist, 47, 360–370.
Viswanathan, K., and Ghose, S. (1965) The effect of Mg^{2+} substitution on the cell dimensions of cummingtonites. American Mineralogist, 50, 1106–1112.
Whittaker, E.J.W., and Zussman, J. (1961) The choice of axes in amphiboles. Acta Crystallographica, 14, 54–55.
Willaime, C., and Brown, W.L. (1974) A coherent elastic model for the determination of the orientation of exsolution boundaries: Application to the feldspars. Acta Crystallographica, A30, 316–331.
Wood, R.M. (1980) Compositional zoning in sodic amphiboles from the blueschist facies. Mineralogical Magazine, 43, 741–752.

Manuscript received January 8, 1990
Manuscript accepted February 26, 1991